SUPPLEMENTARY MATERIAL FOR: BIOINSPIRED FLUIDIC DESIGN FOR ADDITIVE MANUFACTURING

Computational modeling of iCLIP 3D printing

A geometric description of our system is illustrated in **Supplementary Figure 1**. When $\epsilon \ll 1$, the simplified governing lubrication equations for momentum are:

$$\frac{\partial \tilde{p}}{\partial \tilde{z}} \approx 0 \tag{16}$$

$$\tilde{\nabla} \tilde{p} \approx \frac{\partial^2 \vec{\tilde{u}}}{\partial \tilde{z}^2} \tag{17}$$

And from continuity:

$$\tilde{\nabla} \cdot \vec{\tilde{u}} + \frac{\partial \tilde{u}_z}{\partial \tilde{z}} = 0 \tag{18}$$

with the boundary conditions imposed at the part contour $\tilde{p} = 0 \; at \; (x, y) \in \Omega(z)$, $\tilde{u}_z(\tilde{z} = 0) = 0$, and $\tilde{u}_z(\tilde{z} = 1) = 1$. Integrating **Equation 17** gives the dimensionless fluid velocity in the x and y directions as $\vec{\tilde{u}} \approx -\frac{1}{2}\nabla \tilde{p} \tilde{z}(1 - \tilde{z})$ and integrating **Equation 18** gives the dimensionless fluid velocity in z direction as $\tilde{u_z} = -\int_0^{\tilde{z}} \tilde{\nabla} \cdot \vec{\tilde{u}} dz$. The resulting suction force on object P results from the negative pressure required to support the flow as the build platform moves:

$$\tilde{\nabla}^2 \tilde{p} = 12 \tilde{u}_z(\tilde{z} = 1) \tag{19}$$

Integrated over the footprint of the part gives us an approximation of the force required to offset the suction forces. For a cylindrical part of radius R and $\tilde{u_z}(\tilde{z} = 1) = 1$:

$$F_s = -\frac{3\pi \mu U R^4}{h^3} \tag{20}$$

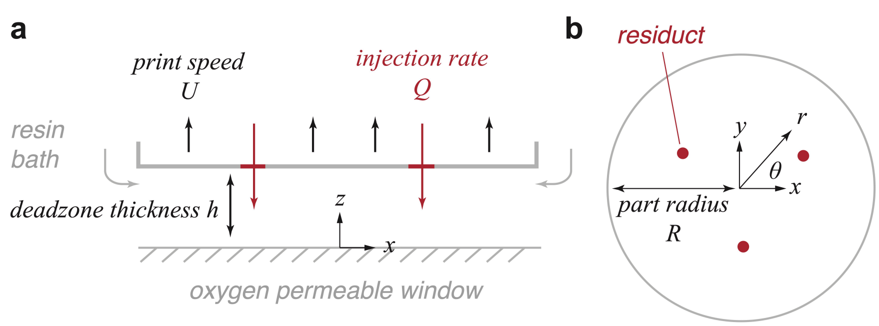

Fig. 1. Geometric description of CLIP deadzone modeled in this work, with print speed U, deadzone height h, and part radius R, where R » h to justify the lubrication approximation.

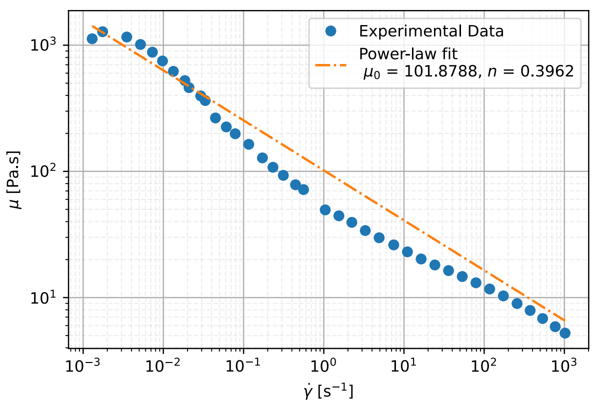

Fig. 2. Apparent viscosity of EPU 40 resin fit to the power-law model from Equation 3.

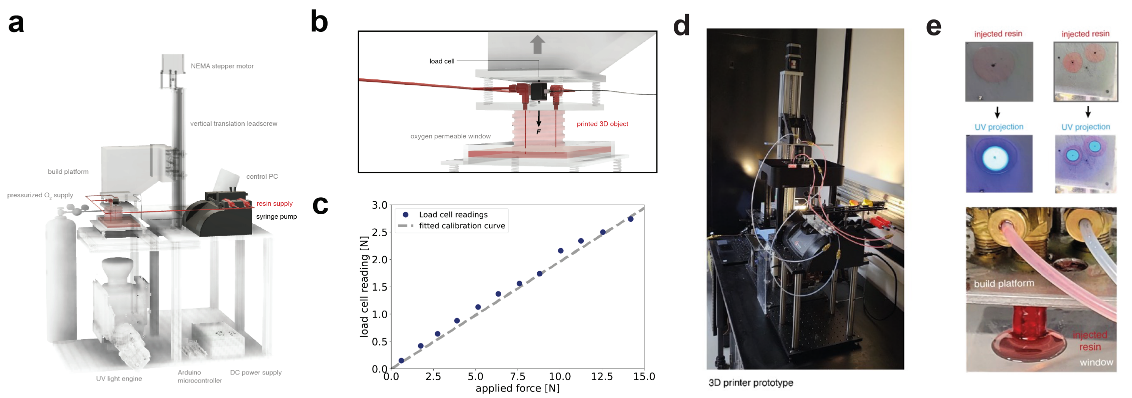

Fig. 3. Summary of hardware modifications to state-of-the-art resin 3D printer for injection 3D printing. (a) schematic of iCLIP printer set-up; (b) mechanism by which load cell records Stefan forces; (c) observed linearity in load cell readings; (d) real-world printer set-up; (e) images taken under the vat during printing with injection.

Materials and Methods

Inverse design algorithm

The overall goal is, for an arbitrary 3D model with potentially many overhangs, to construct a fluidic network that offsets suction at every layer. To generate a suitable 3D printable network to achieve this, we formulate the design task as a path planning optimization problem where, for an arbitrary 3D geometry to be 3D printed via a set of 2D slice layers, we computationally design a corresponding fluidic network that can offset suction forces at all layers. The interconnected node-link nature of this design problem leads to a natural formal representation of the to-be-printed 3D fluidic network as a graph $G \equiv (N, E)$ with nodes $N = \{n_i\}$, where nodes in adjacent layers l and $l+1$ are connected by edges $e \in E = \{e_{ij}\} \subset V \times V$. Such a graph is subject to certain fabrication process constraints. First, the network graph G, which is dynamically growing during printing, should at all layers l be fully connected, with all nodes n reachable by the root note n_0 supplied by the pump; never should a partial network exist with an outlet node n not reachable by

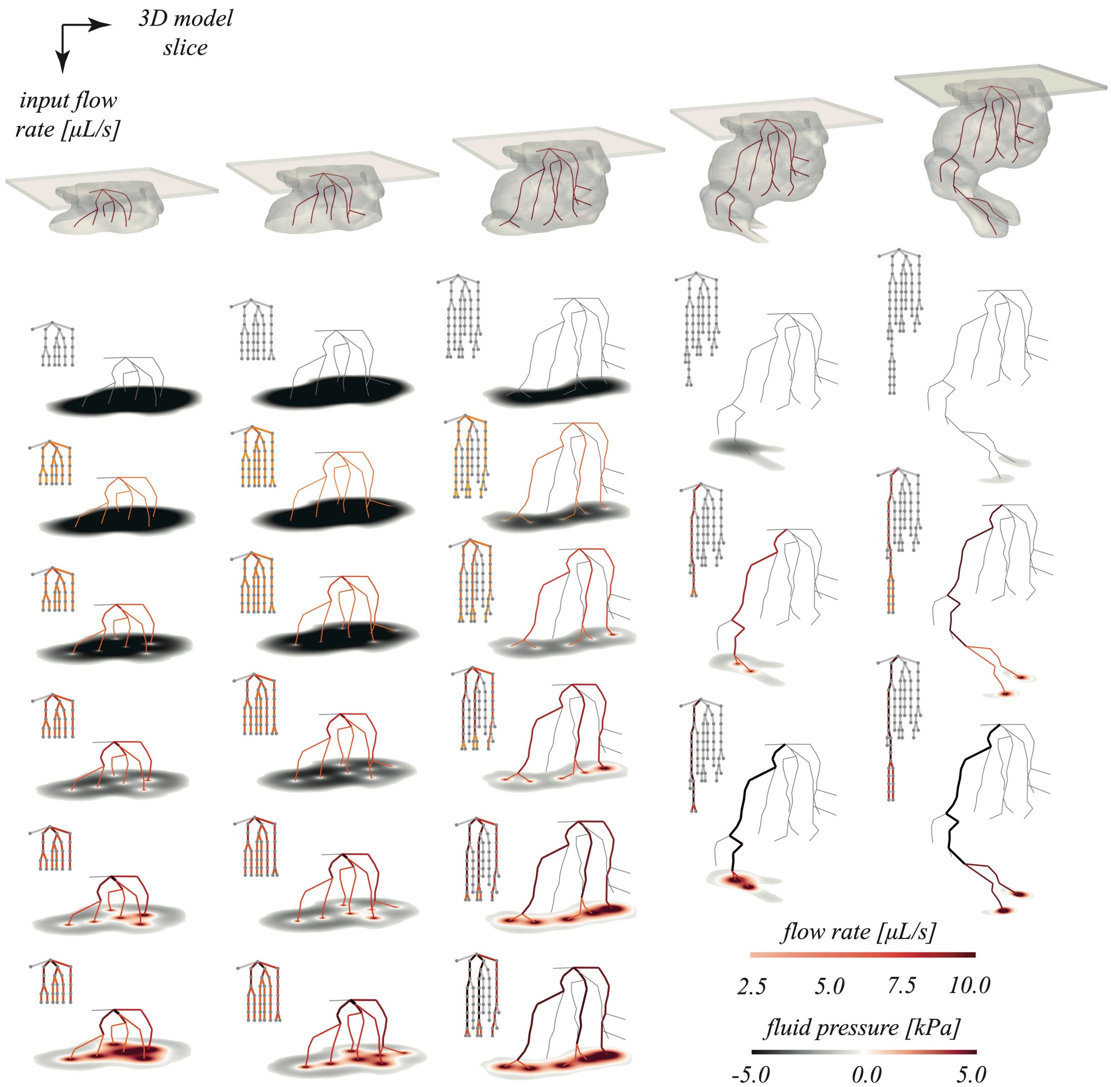

Fig. 4. Deadzone pressure profile modeling. Rows denote the current slice of the printed model, for which fluid pressures as a function of injection rate are predicted, with red and grey indicating higher and lower pressures, respectively.

n_0. Second, the network must be monotonically increasing with respect to the printing axis; otherwise, at given times during fabrication, certain sections of the network would be unreachable by n_0. Third, the resulting fluidic network must be a fully closed system; outlets should only direct flow into the vat, and not external to the part into atmosphere. Finally, at no time should channel radii fall below the minimum negative feature resolution of the 3D printer. In addition, we encode several soft constraints to facilitate the printability of generatively designed networks. First, we minimize network tortuosity to minimize frictional energy loss around sharp corners during pumping. Relatedly, it is desirable

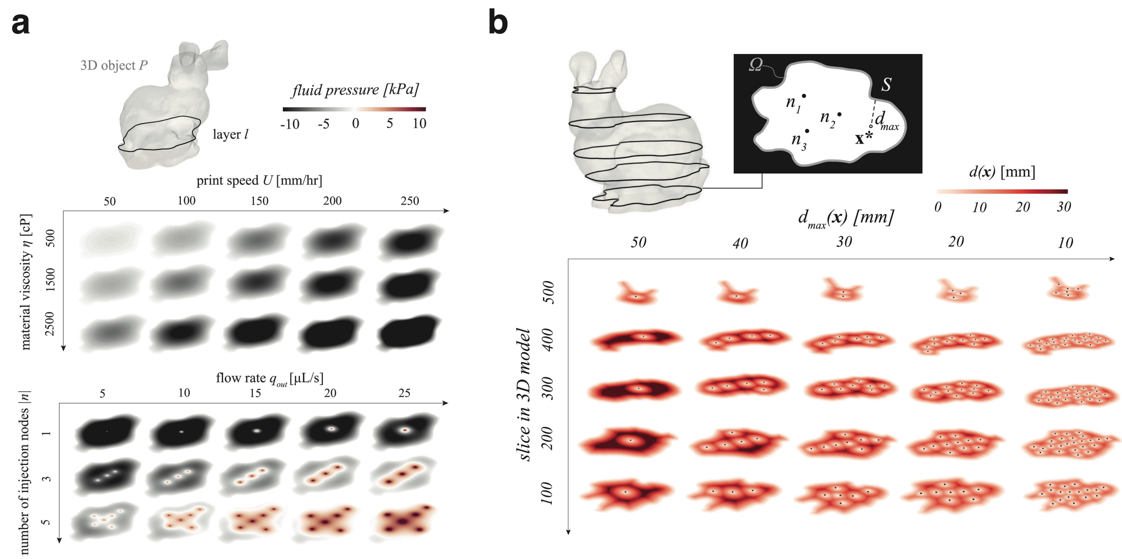

Fig. 5. (a) When a given layer l while printing a 3D object P is considered independently, physical parameters such as print speed U and material viscosity η are positive correlated with failure-inducing suction forces F_s. Injection 3D printing incrementally adding high pressure injection sources n, each with a flow rate q_{out}, can offset such suction. (b) Optimization objective for pressure control during vat 3D printing. Our pipeline minimizes the distance d from any pixel representing a point in the printed object to an input fluid source.

to produce the shortest possible network, given the pump pressure required to drive viscous flow through a fluidic network increases with the total length of the network.

To satisfy these design goal constraints, begin by originating a fluidic network with a single input injection point at the platform. Then, injection channels are positioned within the user-provided model at optimal positions as determined by our deadzone pressure modeling to offset suction during printing, transitioning otherwise negative fluid pressure regions during printing to positive pressure zones. Every time the network is extended with a new branch, the input injection rate from the syringe pump is correspondingly incremented, such that cumulative flow also increases. Branches may be either open (with outlets), or closed (without outlets), thus not contributing to flow. The final network, encoded as a graph connectivity matrix of nodes and edges, is converted to a series of smooth NURBS curves, swept to produce a positive network 3D geometry. Our approach also integrates an evolutionary module [20].

Algorithm 1: GENERATE INITIAL POINTS USING CLUSTERING

Function Generate Initial Points(C): ▷ Irregular contour C
  Initialize a set of random points R within C ▷ Points inside contour
  Cluster R using k-means with $k = 2$ ▷ Form two clusters
  Compute centroids C_1 and C_2 of the clusters ▷ Initial points for optimization
  return C_1, C_2

As the network graph G grows in complexity, it becomes essential to accurately predict flow from the single input source n_0 with a single input flow rate q_{in} to all outlet nodes $\{n\}_l$ in a given layer l with varying outflows $q_{out}(n)$. For

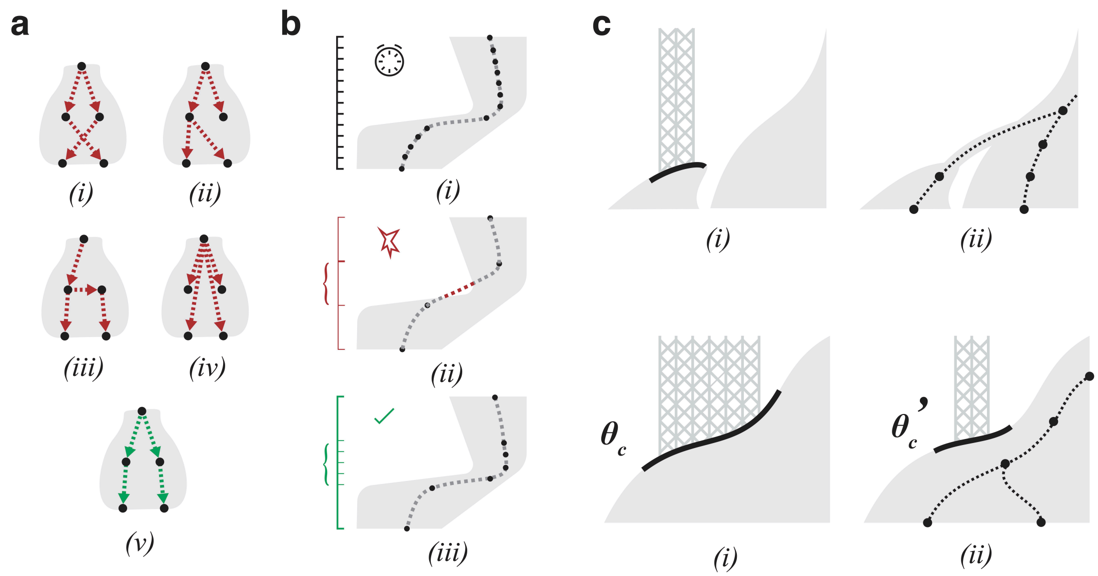

Fig. 6. Design tool integration. (a) Hard constraints on the design space. (b) Adaptive slicing approach. (c) Method for integration of our fluidic approach with support structure generators.

Algorithm 2: DIFFERENTIAL EVOLUTION FOR OPTIMIZING POINT POSITIONS

Function `Optimize Point Positions`(C, C_1, C_2): ▷ `Irregular contour` C, `Initial points` C_1, C_2
  Define objective function f: Cumulative distance of all positions in C to nearest point or contour
  Initialize population with C_1, C_2 and random perturbations ▷ `DE population`
  while *not converged* **do**
    For each individual in the population:
    begin
      Mutate individual using DE strategy ▷ `Generate trial vector`
      Crossover with another individual to produce offspring
      Evaluate offspring using f
      If offspring is better, replace individual ▷ `Selection step`
    end
    Store best individual and its objective function value
    Check convergence criteria
  end
  Extract best positions from the best individual
  return Optimal positions

an accurate and computationally tractable estimate, we model G as an electrical circuit, as is typical for pressure-driven fluidics [22]. Specifically, a corresponding circuit representation is constructed for every dynamic microfluidic network N_t at time t during printing of object P. Importantly, this circuit analogy captures the evolving nature of the network G, where branches b may become closed if their termini are solidified within the object, thus not contributing to fluid flow. In our evolving graph G, this is described by the case when a parent node n in layer l is assigned no child nodes in layer $l+1$, such that node n is a leaf node and the corresponding branch b terminates. In this case, input injection flow q_{in} is redirected to remaining active branches.

Combined with our forward fluid dynamics model, which predicts pressure profiles p and corresponding suction forces F_s for a given layer l with regions S and a distribution of nodes $\mathbf{n}$ and given flow rates from every node $\mathbf{q_{out}}(\mathbf{n})$, this allows us to compute a predicted pressure profile using a vector of potentially varying outflows q_{out} for a given input flow rate q_{in}. Each time a node n is added to a layer l, the input injection rate q_{in} is incremented. We repeat until our termination criterion of zero net fluid suction is satisfied, i.e. $F_s = 0$ at any section S, or formally:

$$n_l, q_{in}(l) \longrightarrow \{|F_s(S)| \leq 0 \;\forall\; S \in l\} \tag{21}$$

This produces a time-dependent syringe pump injection profile $q_{in}(l)$, which can be sent as serial commands over the course of the entire print. Layers l of the part P containing footprints S with larger cross sectional areas require more injection sites $\{n\}_l$ and, correspondingly, higher input injection rates q_{in} to fully offset suction forces F_s.

Having generated an initial network G offsetting suction forces F_s in all 2D cross sections S of 3D part P, we subsequently perform a metaheuristic evolutionary optimization routine to minimize the magnitude of p_{min} in all layers l. Specifically, we implement a genetic algorithm where a candidate solution $\{n\}$ is described by the position of one, or multiple, injection nodes n, and an optimal solution $\{n\}_{opt}$ is that which minimizes $|p_{min}|$. To calculate the location $\mathbf{x}$ of minimum fluid pressure p_{min} for a given part cross section S, it is not necessary to solve for the full fluid pressure distribution $p(\mathbf{x})$ every iteration that positions of nodes $\{n\}$ are updated, which would be computationally expensive. Rather, $p_{min}(\mathbf{x})$ will be located at the point $\mathbf{x}$ in S with the greatest Euclidean distance $d(\mathbf{x})$ to either the part contour Ω or an injection node n:

$$d(\mathbf{x}) = \min\{\|\mathbf{x} - n\|_2 \;\forall\; n \in \mathbf{n}\;, \|\mathbf{x} - \Omega\|_2\} \tag{22}$$

This subdivides S into a number of Voronoi regions [5] equal to $|\mathbf{n}| + 1$ for part cross section S, each specified either by one of $|\mathbf{n}|$ injection nodes in S containing all points closest to node n:

$$V(n_i) = \{\mathbf{x} : d(\mathbf{x}, n_i) \leq d(\mathbf{x}, n') \;\forall\; n' \in N\} \tag{23}$$

or by the part contour Ω supplying fluid via suction and all points closer to Ω than to any node n:

$$V(\Omega) = \{\mathbf{x} : d(\mathbf{x}, \Omega) \leq d(\mathbf{x}, n') \;\forall\; n' \in N\} \tag{24}$$

Illustrative such Voronoi tesselations $V(\mathbf{n}, \Omega)$ for varying layers l in a 3D object are shown, where each node n and part contour Ω in S is assigned a region of closest points $\mathbf{x}$. The objective function to minimize is hence, for every part section S, the maximum distance d_{max} from any point $\mathbf{x}$ to a fluid source, either an injection node n or part contour Ω: $d_{max}(S, \mathbf{n}, \Omega) = \max\limits_{\forall \mathbf{x} \in S} d(\mathbf{x})$.
This equates to minimizing the negative fluid pressure $|p_{min}|$:

$$\{n\}_{opt} = \underset{\{n\}}{\operatorname{argmin}}\; |p_{min}(\mathbf{x})| \tag{25}$$

The final network G representing the fluidic system, encoded as a graph connectivity matrix of nodes and edges, is converted to a series of smooth NURBS curves. This parametric CAD is swept to produce a positive network 3D geometry, and finally Boolean differenced with the original B-rep CAD model via surface-to-surface intersection [29] to produce negative channels, hence an innervated part P'. While there is one optimal network that minimizes $|p_{min}|$, many feasible network configurations may both offset suction F_s for all layers l, while satisfying the design space constraints described above. Formally the solution set of potential networks G with a fluid pressure threshold p_{min} is described by:

$$\{G\} = \{G \rightarrow \ \forall\, \mathbf{x} \in P,\ p(\mathbf{x}) > p_{min}\} \tag{26}$$

with an optimum that minimizes suction force F_s:

$$G_{opt} = \underset{G \in \{G\}}{\operatorname{argmin}} \sum_{l} F_s(l) \tag{27}$$

Experimental validation

As illustrated in **Supplementary Figure 10a**, we assess an overhang represented as the cables of the Golden Gate bridge, which possesses a *macro-mini* structure: in a single part footprint, some cross sections possess high areas (main body of the cable), whereas other ornamental details are significantly smaller (cable ropes). We note that these slender elements are *not* connected to the build platform, and instead extend downwards from the part; hence, they do not act as supporting members for the geometry's main element. Even if the cross sectional area of these smaller regions in an object footprint is small, if any region in the growing part suffers from suction-related failure, then the resulting layer shift defects may disrupt successful printing of all regions. This is shown for the inset detail of the bridge cable ornament, where if printed unsupported significant layering is observed, caused by the torque exerted at the high cross section of the main bridge cable, as for the rod. These defects can be prevented by support structures, as illustrated in the schematic, but at the cost of significant material waste. To compare results between the traditional approach and our method, we hold all print conditions constant save for the co-design of fluidic networks for injection. CT scans of the printed bridges illuminate the channels embedded within the printed geometry. As for the case of the rod primitive above, no layering defects manifest in the main body of the cable, i.e. the largest cross section of the printing object. The ornamental details, i.e. smaller cross sections, are also perfectly resolved in these prints.

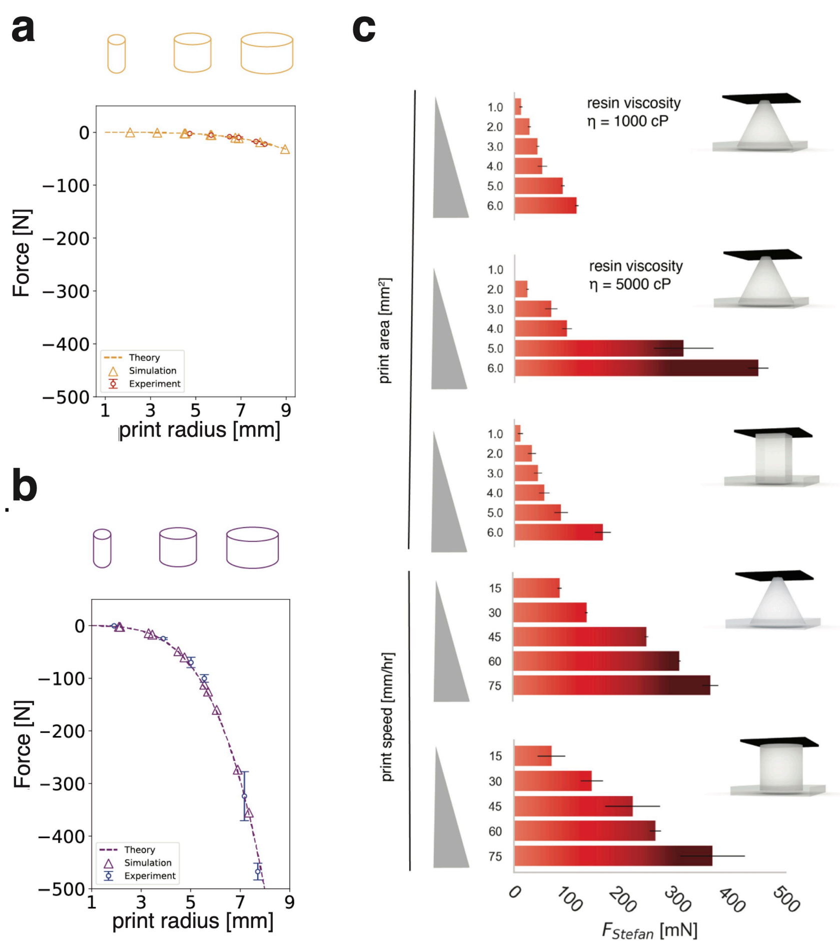

Fig. 7. Force reading without injection dependence on geometry and material rheology. Measured Stefan forces while printing geometries with circular cross section (a). For cone of varying radius within a single print, and for cylinder of varying radius between prints with resin of viscosity 500 cP (a) and 1800 cP (b). (c) Multiparameter sweep experiments quantifying the impact of (i) part cross sectional area, (ii) resin viscosity, and (iii) print speed on Stefan force.

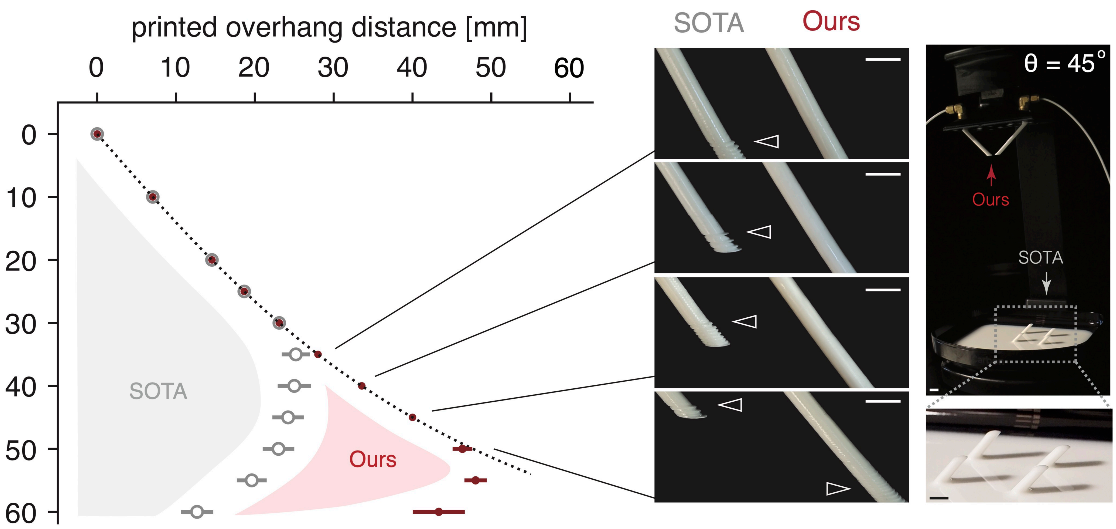

Fig. 8. Experimental validation of our approach with primitive geometries. Print results for varying overhang angles by SOTA and our approach for rod geometries. Error bars denoting +/- one standard deviation from mean of technical triplicates. White arrows denote suction-related defects. Scale bars indicate 5 mm.

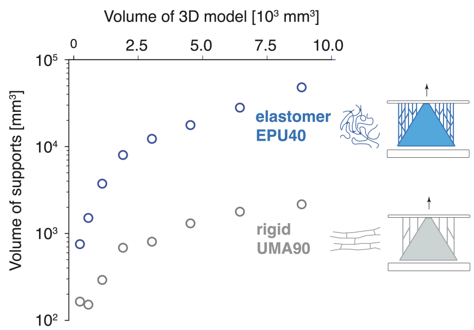

Fig. 9. Using a commercial slicer from [3], volume of supports required as a function of cone model volume for both rigid (UMA90) and elastomeric (EPU40) resins considered in this work.

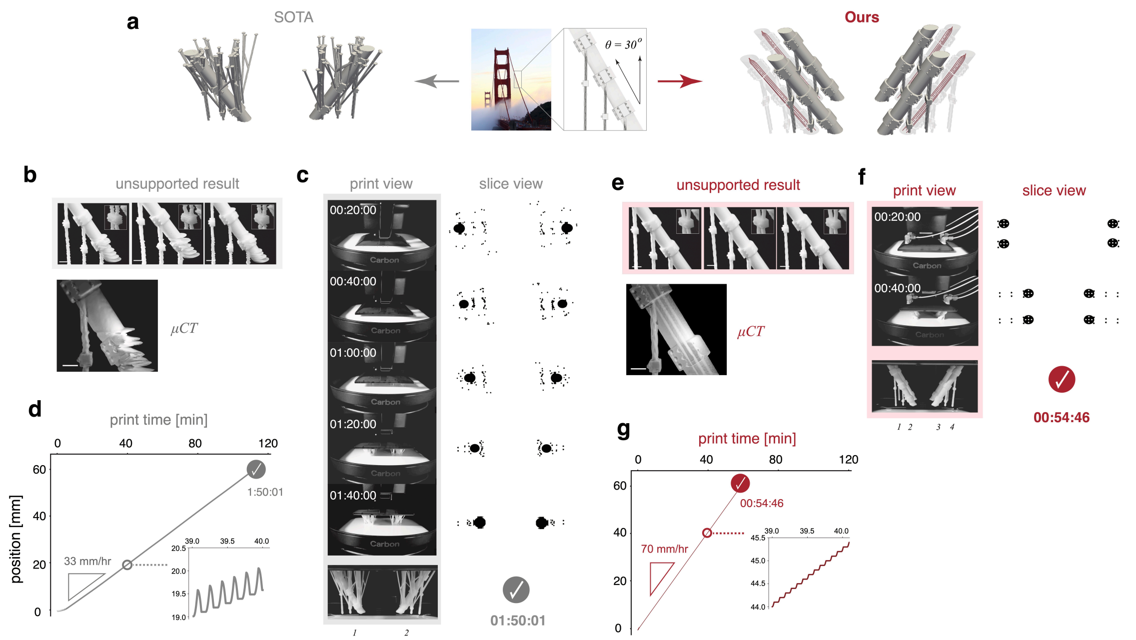

Fig. 10. Experimental validation of our approach with complex geometries. (a) CAD model with overhang considered, with support requirements for SOTA and network requirements for our approach. Unsupported print results for SOTA (b), and recommended print speeds with fabrication timestamps underneath, (c) and print kinematic scripts prescribed for SOTA (d). Unsupported print results for approach (e), and achievable print speeds with fabrication timestamps underneath (f) and print kinematic scripts prescribed for our approach (g). Full timelapses available in **Supplementary Video 3**. Scale bars denote 5 mm.

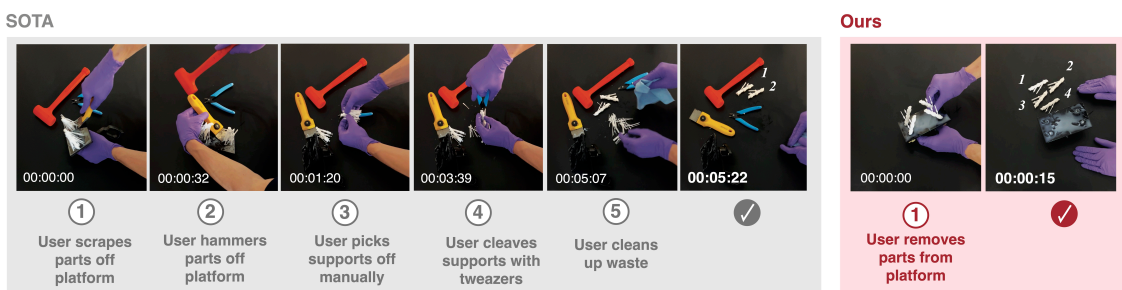

Fig. 11. Summary of post-processing procedures for traditional 3D printing with support structures (left) and for our approach (right).

Table 1. Experimentally-demonstrated print throughput and efficiency for three test models by SOTA and by our method. All prints were performed with UMA90 resin from Carbon3D.

	Bridge		*Sculpture*		*Statue*	
	SOTA	Ours	SOTA	Ours	SOTA	Ours
Model geometry						
Prints per platform	2	4	1	2	2	4
Linear speed [mm/hr]	33	70	33.5	55.7	33.6	66.3
Support geometry						
Volume [mL] (% part volume)	4.3 (44%)	0 (n/a)	4.1 (24%)	1.3 (7.9%)	3.0 (13.8%)	0.8 (3.5%)
Cumulative						
Unit cost [$ / L] †	**370**	**260**	**290**	**270**	**325**	**280**
Throughput [mL/hr] ‡	**10.8**	**43.2**	**8.7**	**41.7**	**13.2**	**57.1**

† Calculated as resin price per 3D model volume, including supports.
‡ Calculated as 3D model volume printed per unit time.

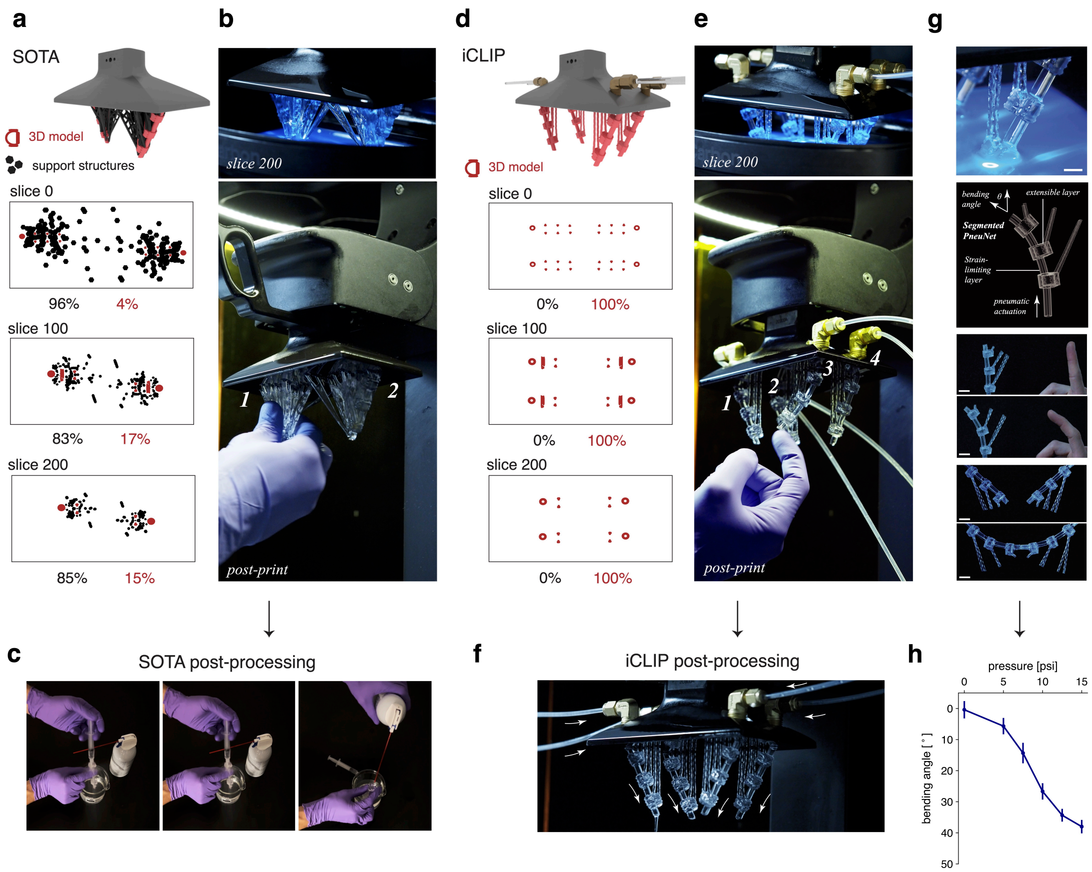

Fig. 12. Soft robotics application of iCLIP printing. (a) By state-of-the-art printing, an example bending actuator requires support structures indicated in **black**, with model itself in red, which provides structural stiffness to the object during printing (b). (c) After printing, as for cleaving supoports, cleaning procedures are highly manual. (d-e) During iCLIP printing, no supports are needed, liberating space on the platform for more parts. (f) After printing, such channels can be readily cleaned by the same fluidic system used for injection during printing. (g-h) For the PneuNet printed by our method, fluid pressure exerted through embedded channels is positively correlated with the bending angle of the soft actuator.